X International Conference on Computational Methods in Marine Engineering
MARINE 2023
J. García-Espinosa, L. González, J.E. Gutiérrez & B. Serván-Camas (Eds)

Application of a two-step fluid-structure approach for the analysis of large deformations and linear vibrations of propeller blades with embedded viscoelastic material

Quentin Rakotomalala[1,2*], Lucie Rouleau[2], Cédric Leblond[1], Mickael Abbas[3], Jean-François Deü[2]

[1] Centre d'Expertise des Structures et Matériaux Navals, Naval Group, Technocampus Océan, 44340 Bouguenais, France, e-mail: quentin.rakotomalala@naval-group.com, cedric.leblond@naval-group.com

[2] Laboratoire de Mécanique des Structures et des Systèmes Couplés (LMSSC) Le Cnam, 2 rue Conté, 75003 Paris, e-mail: lucie.rouleau@lecnam.net, jean-francois.deu@lecnam.net

[3]Electrotechnique et Mécanique des Structures (ERMES), Electricité de France (EDF), 7 boulevard Gaspard Monge, 91120 Palaiseau France, e-mail: mickael.abbas@edf.fr

[*] Corresponding author: Quentin Rakotomalala, quentin.rakotomalala@naval-group.com

ABSTRACT

In this paper, a simplified numerical approach is applied to the analysis of the linear vibrations of aluminum or composite marine propeller blades with embedded viscoelastic films, around a predeformed nonlinear state. This approach allows to evaluate in a sequential way the nonlinear deformation, induced by the generation of lift (propulsion phenomenon), and the acoustic power emitted (vibro-acoustic phenomenon) of a non-cavitating flexible marine propeller blade. For a given incident flow, the deformation of an aluminum blade is much smaller than that of a composite blade. The composite blade's deformation has a significant positive impact on lift generation whereas the deformation of the aluminum blade tends to reduce traction. The dynamic characteristics of the aluminum blade at rest and under the fluid induced static load are similar, while those of the composite blade are very different in these two cases. The simplified two-step approach proposed in this study is therefore useful to accurately assess the emitted sound power by the vibrating blades.

Keywords: fluid-structure interaction, large deformation, pre-stressed state, vibroacoustic, blade element method, finite element method. viscoelastic material

Nomencalture

$\mathcal{C}_0$	Initial configuration	$\boldsymbol{\sigma}_1$	Propulsion Cauchy stress tensor [Pa]
$\mathcal{C}_1$	Intermediate configuration	$\boldsymbol{u}$	Displacement field between $\mathcal{C}_0$ and $\mathcal{C}_2$ [m]
$\mathcal{C}_2$	Actual configuration	$\boldsymbol{u}_1$	Displacement field between $\mathcal{C}_0$ and $\mathcal{C}_1$ [m]
c	Speed of sound in the fluid [m/s]	$\boldsymbol{u}_2$	Displacement field between $\mathcal{C}_1$ and $\mathcal{C}_2$ [m]
p	Fluid pressure [Pa]	$\boldsymbol{v}$	Fluid velocity [m/s]
p_1	Propulsion fluid pressure [Pa]	$\boldsymbol{v}_1$	Propulsion fluid velocity [m/s]
p_2	Vibro-acoustic fluid pressure [Pa]	$\boldsymbol{M}$	Structural mass matrix

ρ	Fluid density [kg/m^3]	$\boldsymbol{G}$	Fluid mass matrix
ρ_s	Structural density [kg/m^3]	$\boldsymbol{C}$	Fluid structure coupling matrix
ψ_2	Vibro-acoustic fluid potential velocity [m^2/s]	$\boldsymbol{H}$	Fluid stiffness matrix
$\boldsymbol{\sigma}_2$	Vibro-acoustic pseudo Cauchy stress tensor [Pa]	$\boldsymbol{K}^{\tan}$	Structural tangent stiffness matrix
		$\boldsymbol{Q}$	Impedance matrix

1. Introduction

Whether it comes from the hydrodynamic boundary layer pressure fluctuation or engine and shaft excitation, propeller blades vibrate and emit noises. A warship must keep its noise level as low as possible in order to avoid detection in combat. Civilian ships also have an interest to maintain low noise emission as it can be harmful to the marine environment. Therefore stealth is still a major design challenge for today's ships. By transforming vibrational energy into heat, viscoelastic films can be inserted in the structure to severely reduce the radiated noise [Rouleau et al., 2012], [Leblond and Sigrist, 2016]. The computation of noise level emitted propeller's blades has numerous challenges as many physical phenomena are involved: the rotating blades generate lift and suffer a displacement which can be significant [Taketani et al., 2013], the pressure field associated with noise is a compressible phenomenon and the damping properties of the viscoelastic material depend on their state of pre-strain and pre-stress.

In this work, the fluid is considered as non cavitating and the rotation velocity is constant and much smaller than the lowest vibration frequency studied. Two main phenomena are identified:

- The propulsion phenomenon, which takes into account the fluid-structure interaction between the deformable blade and the rotating incoming static flow that leads to lift generation and structural deformation.
- The vibro-acoustic phenomenon, which involves the noise propagation due to the vibration of the pre-stressed blade. The vibration amplitude of the structure is considered small therefore this problem can be linearized.

The proposed approach allows to split the non-linear fully coupled dynamic problem into two chained problems:

- a nonlinear, stationary and coupled problem which allows computing the deformation and the prestress into the rotating blade under fluid flow (propulsion problem);
- a vibro-acoustic problem to compute the noise radiated by the linearized vibrations of the pre-deformed and prestressed blade.

The simplified approach is used to study the deformation under lift generation and the vibration characteristics of two blades. The first blade is made of aluminum and the second is made of carbon epoxy composite plies. A damping material is embedded at the core of both blades. Since the vibro-acoustic phenomenon is studied on a narrow frequency range, the mechanical characteristics of the damping layer are taken into account using a simplified viscoelastic model with constant average properties.

2. Phenomena separation and simplification

2.1 Equations of the phenomena

The following regime is considered:

- the length of the blade L_0 is over 1 m;
- to avoid cavitation, the velocity at blade tip is limited: $L_0\omega_p \lesssim 40$ m.s^{-1} where the propeller rotation speed ω_p is considered constant.;
- the incident velocity $\boldsymbol{v}_\infty$, which is linked to the vessel's speed is of the order of 10 m.s^{-1}, it is also considered constant;
- the frequency of vibration ranges within [100 Hz, 5 kHz], therefore the associated angular frequency $2\pi f \gg \omega_p$.

The turbulence, cavitation and flow induced noises are out of the scope of this work. However such phenomena are of interest for the determination of marine propeller's blade noise emission and would need specific studies. Under the previous assumptions, two main phenomena can be identified and partially decoupled. The first phenomenon will be called the *propulsive phenomenon*, it is responsible for the lift generation on each blade and the propulsion of the ship. In a general setting, the displacement of the structure can be high enough [Taketani et al., 2013], [Muller and Pécot, 2017] so that a non-linear structure model is required. The velocity of the fluid is of the order of $\boldsymbol{v}_\infty$ therefore highly subsonic and the fluid can be considered incompressible. The second phenomenon, which is called *vibroacoustic phenomenon* takes into account small vibrations of the pre-stressed structure. These vibrations generate pressure waves of small amplitudes into the fluid, therefore this phenomenon can be considered linear and will be studied in the Fourier space. Figure 1 shows the different configurations. The propulsion phenomenon and the vibro-acoustic phenomenon have different orders of magnitudes.

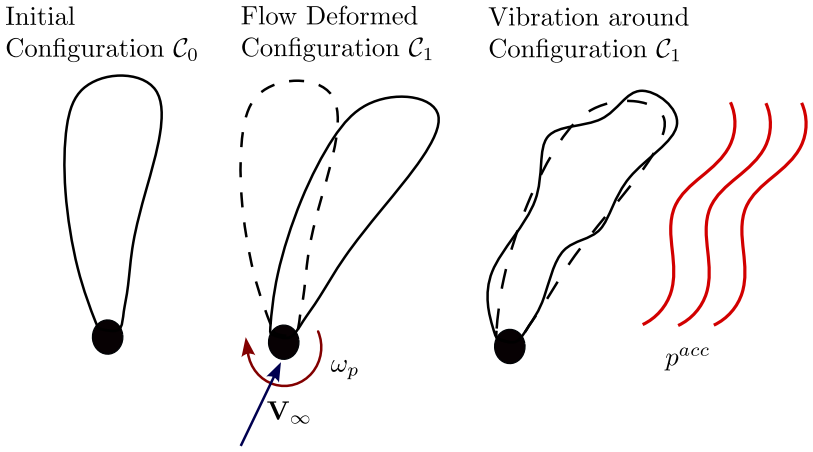

Figure 1: The 3 configurations (initial, intermediate, actual) of the propeller

Each quantity $\chi \in [\boldsymbol{u}, \boldsymbol{v}, p, \rho]$ is split into a propulsion contribution χ_1 and a vibro-acoustic contribution χ_2. The structural, fluid and boundary condition equations can be simplified by performing an asymptotic expansion on χ_2 at χ_1. The order 0 in χ_2 gives the propulsion equation and the order 1 in χ_2 gives the vibro-acoustic equations.

In the specific regime studied in this article, the propulsion equation on configuration $\mathcal{C}_1$, reads:

$$\left\{\begin{array}{rcll} \rho\left((\boldsymbol{v}_1\cdot\nabla)\boldsymbol{v}_1+2\omega_p\boldsymbol{R}\boldsymbol{v}_1+(\omega_p\boldsymbol{R})^2\boldsymbol{x}\right) &=& -\nabla p_1 & \text{in } \Omega^f \\ \nabla\cdot\boldsymbol{v}_1 &=& 0 & \text{in } \Omega^f \\ \rho_s(\omega_p\boldsymbol{R})^2\boldsymbol{x}_1 &=& \nabla_1\cdot\boldsymbol{\sigma}_1 & \text{in } \Omega^s \\ \boldsymbol{\sigma}_1\boldsymbol{n}_1 &=& -p_1\boldsymbol{n}_1 & \text{on } \partial\Omega^s \\ 0 &=& \langle\boldsymbol{v}_1,\boldsymbol{n}_1\rangle & \text{on } \partial\Omega^s \\ \lim_{\|\boldsymbol{x}\|\to\infty}\boldsymbol{v}_1+\omega_p\boldsymbol{R}\boldsymbol{x} &=& \boldsymbol{v}_\infty & \end{array}\right. \tag{1}$$

where the matrix $\boldsymbol{R}$ is the linear rotation operator: $\boldsymbol{x}\mapsto\boldsymbol{e}_z\wedge\boldsymbol{x}$. The vibro-acoustic equation on configuration $\mathcal{C}_1$ in a $u-\psi$ formalism are written as follow:

$$\left\{\begin{array}{rcll} \rho_s\omega^2\boldsymbol{u}_2+\nabla_1\cdot\boldsymbol{\sigma}_2 &=& 0 & \text{in } \Omega^s \\ \left(\frac{\omega}{c}\right)^2\psi_2+\Delta\psi_2 &=& 0 & \text{in } \Omega^f \\ i\omega\langle\boldsymbol{u}_2,\boldsymbol{n}\rangle &=& \langle\nabla\psi_2,\boldsymbol{n}\rangle & \text{on } \partial\Omega^s \\ \boldsymbol{\sigma}_2\boldsymbol{n} &=& i\omega\rho\psi_2\boldsymbol{n} & \text{on } \partial\Omega^s \\ \boldsymbol{\sigma}_2\boldsymbol{n} &=& -p^{\text{excit}}\boldsymbol{n} & \text{on } \Gamma^{\text{excit}} \end{array}\right. \tag{2}$$

where p^{excit} is the excitation pressure applied on a surface Γ^{excit} of the blade. And $\boldsymbol{\sigma}_2=\boldsymbol{\sigma}_2^{\text{m}}+\boldsymbol{\sigma}_2^{\text{g}}$ is the linearized stress tensor written on configuration $\mathcal{C}_1$ which has two contributions:

- the material stress $\boldsymbol{\sigma}_2^{\text{m}}$ which takes into account nonlinear behaviour law of the material via the differential of $\boldsymbol{S}$.
- the geometrical stress $\boldsymbol{\sigma}_2^{\text{g}}$ accounting for the pre-stress of the structure.

2.2 Resolution of the two phenomenon

These two phenomena can be solved sequentially. The non-linear, stationary propulsion phenomenon is solved first. It gives the pre-stress and pre-strain as input to the vibro-acoustic phenomenon that is solved in the Fourier space at multiple frequencies.

2.3 Propulsion phenomenon resolution

In order to solve the propulsion phenomenon, a fully coupled non-linear fluid-structure equations set must solved, it can be symbolically written:

$$\left\{\begin{array}{rcl} p_1 &=& \mathcal{F}(\boldsymbol{u}_1) \\ \boldsymbol{u}_1 &=& \mathcal{S}(p_1) \end{array}\right. \tag{3}$$

where $\mathcal{F}$ (respectively $\mathcal{S}$) is the fluid (respectively structural) solver used to solve equation 1.

As the fluid load depends on the geometry of the blade and the blade displacement depends on the loading from the fluid, the fluid and structure equations must be solved by taking into account this strong coupling. An iterative Neumann-Neumann algorithm is used, as showed in Figure 2, the solution $(\boldsymbol{u}_1,p_1)$ is approached by a sequence $(\boldsymbol{u}_1^k,p_1^k)$ defined by: $\boldsymbol{u}_1^0=0$, $(\boldsymbol{u}_1^k,p_1^k)=(\mathcal{S}(p_1^k),\mathcal{F}(\boldsymbol{u}_1^{k-1}))$

The iterations are stopped when the relative error $\|\boldsymbol{u}_1^k-\boldsymbol{u}_1^{k-1}\|/\|\boldsymbol{u}_1^{k-1}\|$ is smaller than a given tolerance $\epsilon=10^{-5}$. If this sequence is convergent, its limit is solution of the fluid-structure coupled problem. In the case of the propulsion phenomenon, this algorithm converges in a few iterations (typically less than 15).

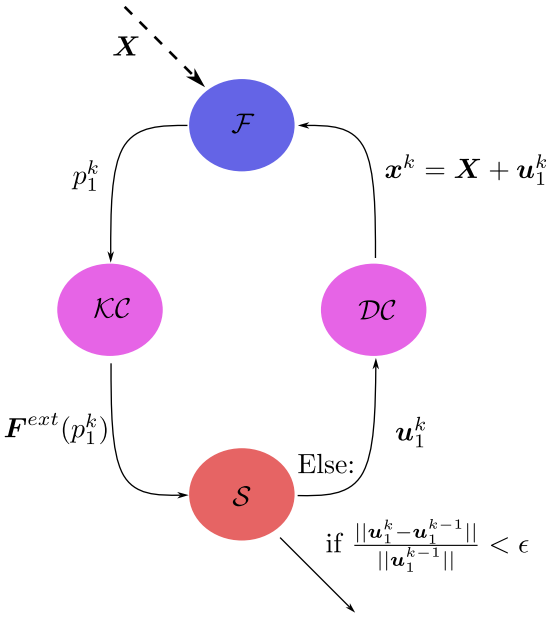

Figure 2: Iterative Neumann-Neumann fluid-structure solver algorithm

In this work, the structural part is solved using the FEM code Code_Aster [EDF, 1989] and the fluid part is solved using a in-house solver based on the blade element method [Glauert, 1935] and Xfoil's panel method [Drela, 1989]

2.4 Vibro-acoustic phenomenon resolution

The vibroacoustic phenomenon Equations 2 can be solved with finite element method in a monolithic $u - \psi$ formulation [Everstine, 1981]. To take into account an infinite fluid domain, the BGT [Bayliss et al., 1982] conditions are used on the boundary Γ_∞ of the spherical fluid domain of radius R:

$$\langle \nabla \psi_2, \boldsymbol{n}_1 \rangle + \left(\frac{i\omega}{c} + \frac{1}{R} \right) \psi_2 = 0 \tag{4}$$

The monolithic $u - \psi$ finite element method is used to solves the weak formulation of the problem on configuration $\mathcal{C}_1$:

- Find $\boldsymbol{u}_2$, such as:

$$-\omega^2 \int_{\Omega^s} \rho_s \langle \boldsymbol{u}_2, \boldsymbol{\delta u} \rangle + \int_{\Omega^s} \boldsymbol{\sigma}_2 : \nabla \boldsymbol{\delta u} + i\omega \int_{\partial\Omega^s} \rho \psi_2 \langle \boldsymbol{\delta u}, \boldsymbol{n} \rangle = \int_{\Gamma^{\text{excit}}} p^{\text{excit}} \langle \boldsymbol{\delta u}, \boldsymbol{n} \rangle \text{ for all } \boldsymbol{\delta u} \tag{5}$$

- Find ψ_2, such as:

$$-\omega^2 \int_{\Omega^f} \frac{\rho}{c^2} \psi_2 \delta\psi + \int_{\Omega^f} \rho \nabla\psi_2 \nabla\delta\psi + \left(i\omega + \frac{c}{R} \right) \int_{\Gamma_\infty} \frac{\rho}{c} \psi_2 \delta\psi - i\omega \int_{\partial\Omega^s} \rho \langle \boldsymbol{u}_2, \boldsymbol{n}_1 \rangle \delta\psi = 0 \text{ for all } \delta\psi \tag{6}$$

These two equations in weak form give the following symmetric matrix system of equations:

$$\left[-\omega^2 \begin{pmatrix} \boldsymbol{M} & \boldsymbol{0} \\ \boldsymbol{0} & -\boldsymbol{G} \end{pmatrix} + i\omega \begin{pmatrix} \boldsymbol{0} & \boldsymbol{C} \\ \boldsymbol{C}^T & -\boldsymbol{Q} \end{pmatrix} + \begin{pmatrix} \boldsymbol{K}^{\tan}(\mathbf{U}_1) & \boldsymbol{0} \\ \boldsymbol{0} & -\boldsymbol{H} - \frac{c}{R}\boldsymbol{Q} \end{pmatrix} \right] \begin{pmatrix} \mathbf{U}_2 \\ \boldsymbol{\Psi}_2 \end{pmatrix} = \begin{pmatrix} \mathbf{P}^{\text{excit}} \\ \boldsymbol{0} \end{pmatrix} \tag{7}$$

The structural stiffness matrix is the tangent matrix $\boldsymbol{K}^{\tan}(\mathbf{U}_1)$ computed at displacement field $\boldsymbol{U}_1$, this term takes into account the pre-stress and pre-strain generated by the propulsion phenomenon. It can be split into two contribution: $\boldsymbol{K}^{\tan}(\mathbf{U}_1) = \boldsymbol{K}_e^{\tan}(\mathbf{U}_1) + (1 + i\eta)\boldsymbol{K}_v^{\tan}(\mathbf{U}_1)$ where $\boldsymbol{K}_e^{\tan}(\mathbf{U}_1)$ is the stiffness matrix of the elastic material and $\boldsymbol{K}_v^{\tan}(\mathbf{U}_1)$ is the stiffness matrix of the viscoelastic material, η is the loss mean factor of the damping layer on the considered frequency range.

3. Numerical application

This procedure is used in order to study a simplified propeller's blade. The blade is one meter long with NACA0006 sections. The chord of the sections varies in a linear way: the root is 250 mm long and the blade tip is 75 mm long. The geometry of the blade is fairly simple but remains representative of a real propeller blade. Figure 3a shows the CAD of the blade.

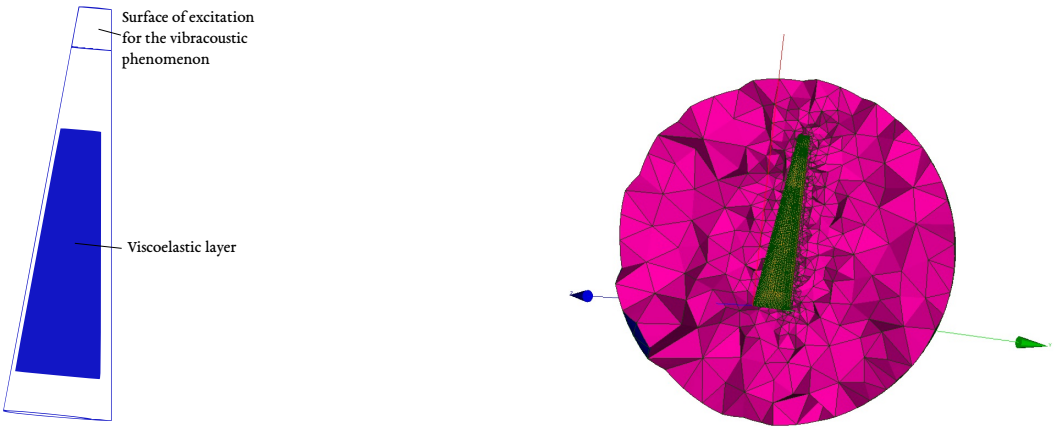

(a) CAD of the blade, the viscoelastic material is embedded at the core

(b) Base mesh for vibroacoustic computation and from which the submesh of the blade is extracted

Figure 3: CAD and base mesh of the blade

Two blades made of different materials are considered: a composite blade made of carbon-epoxy woven fabrics (with fibers aligned at $-45/+45°$ regarding the wingspan axis) and a metallic blade made of aluminum. Both blades have a viscoelastic patch whose size and position are showed in Figure 3a. Table 2 shows the properties of the materials. Both blades suffer the same incident flow characterized by a ship's velocity of $v_\infty = 5$ m.s^{-1} and a rotation speed of $\omega_p = 0.58$rad.s^{-1}

The hub is 0.2 m long, therefore the angle of attack at the blade tip is 8 degrees. This angle is below the stall limit so the flow is unseparated. The harmonic excitation is simplified in this numerical application: a uniform pressure is applied to one side of the blade on a small surface near the tip.

A common base mesh is used for the computation on the aluminum and composite blade. It is made of $\sim 70.\ 10^3$ nodes, $\sim 50.\ 10^3$ 10-nodes tetrahedral elements, 149 20-nodes hexahedral elements and 374 13-nodes pyramids. It is displayed in Figure 3b .

First, the propulsion phenomenon is studied. Computations on the aluminum and composite blades are compared to a fluid computation carried out on a rigid blade. The structure mesh is extracted from the base mesh and 101 hydrodynamic sections are used for the fluid solver. Then the vibroa-

Table 2: Material and fluid properties of the test case.

Water		Aluminum		Composite		Viscoelastic layer	
ρ	1000 kg.m^{-3}	Constitutive law: Saint-Venant-Kirchhoff				Constitutive law: Mooney Rivlin	
c	1500 m.s^{-1}	E	65 GPa	E_1	65 GPa	C_{10}	0.238 MPa
		ν	0.36	E_2	65 GPa	C_{01}	0.523 MPa
		ρ_s	2500 kg.m^{-3}	E_3	10 GPa	K	2.2 GPa
				G_{12}	5 GPa	ρ_s	1400 kg.m^{-3}
				G_{23}	3 GPa	η	0.21
				G_{13}	3 GPa		
				ν_{12}	0.04		
				ν_{23}	0.2		
				ν_{13}	0.2		
				ρ_s	1500 kg.m^{-3}		

acoustic phenomenon is studied. For both the composite and the aluminum blade, the vibro-acoustic computations are carried out on the initial configuration $\mathcal{C}_0$ and on the intermediate configuration $\mathcal{C}_1$ (see Figure 1). The mesh of configuration $\mathcal{C}_1$ is computed using the pseudo material method [Boncoraglio et al., 2021].

3.1 Propulsion phenomenon analysis

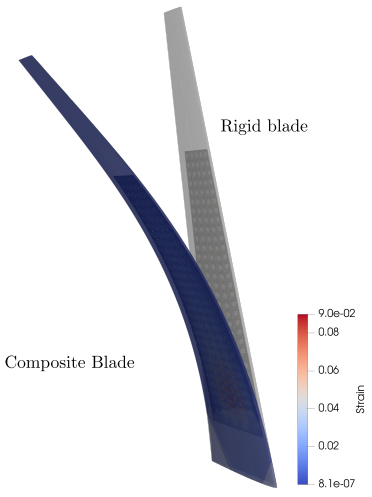

(a) Deformed composite blade with a shear strain color map and rigid blade without color map

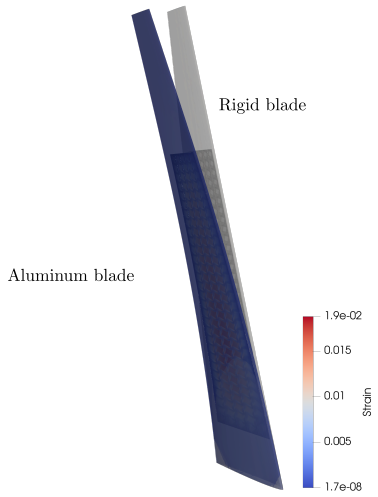

(b) Deformed aluminum blade with a shear strain color map and rigid blade without color map

Figure 4: Shear strain and displacement field of the aluminum and composite blade with the same scale

Figure 4a (respectively Figure 4b) shows the global displacement and deformation fields of the composite blade (respectively aluminum blade). The general motion is a flexion of the blades, the deflection is much more important in the case of the composite blade. In both cases, the shear strain is maximal in the viscoelastic layer, with a maximum shear strain of 9% in the composite blade and 1.9% in the aluminum blade.

The deformation and displacement fields of the composite and aluminum blade is also studied at the section level. To measure the true deformation of the section, the normalized section is analyzed. It corresponds to a section normalized by its chord and represented with its leading edge put at the origin and its trailing edge at point $(1, 0)$. Figure 5a shows the normalized profil at mid blade. The true deformation of the aluminum blade is very small, a tiny positive camber is added to the section but this effect remains marginal. The composite blade on the other hand shows a significant increase in camber.

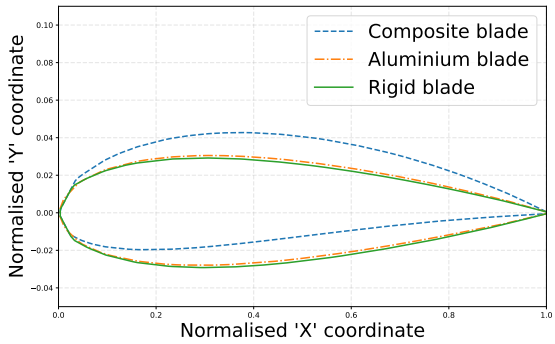

(a) True deformation of the normalized mid section on the aluminum blade, the composite blade and the rigid blade as reference

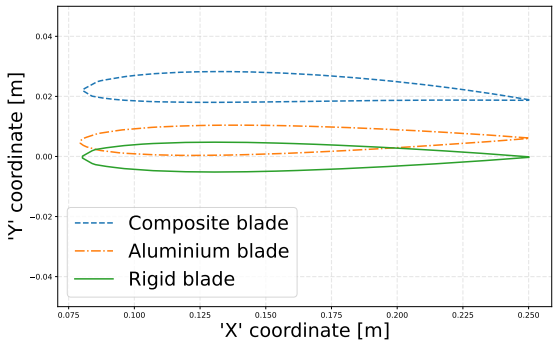

(b) Full deformation of the normalized mid section on the aluminum blade, the composite blade and the rigid blade as reference

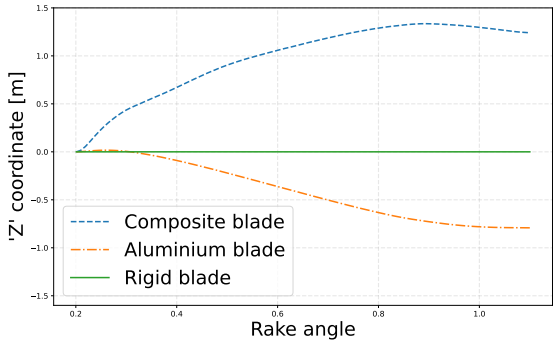

(c) Blade angle of the different sections for the aluminum blade, the composite blade and the rigid blade as reference

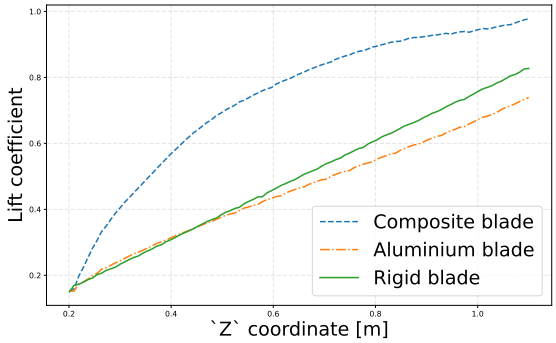

(d) Dimensionless local lift coefficient along the blade's wingspan for the coupled and chained computation

Figure 5: Effect of the fluid/structure interaction on the structural deformation

Figure 5b shows the total deformation, highlighting the flexion of the blades at a given section level. Figure 5c shows the evolution of the blade angle along the wingspan. The rigid blade has a zero blade angle for each section as expected. The deformation of the aluminum blade leads to a slightly positive blade angle at the root and then a significantly negative blade angle toward the tip. The composite blade deformation leads to a positive blade angle. The deformation induces a small torsion in both cases. Overall, the deformation of the composite blade and that of the aluminum blade have very different hydrodynamic implications. On one hand, the deformation of the composite blade leads to a significant camber increase and generates a positive blade angle which are positive for both lift generation. On the other hand, the deformation on the aluminum blade leads to a negligible camber change and an overall negative blade angle which is negative for lift generation.

Figure 5d shows the evolution of the coefficient of lift C_L along the wingspan. In the case of the rigid blade, the angle of attack α at each section z is $\arctan(z\omega/V_\infty) \sim z\omega/V_\infty$. In the attached flow regime, the NACA 0006 lift coefficient can be approached by $C_L = 2\pi\alpha$. Figure **??** shows a load on a rigid blade almost linear with z coordinate, as it is expected. The local lift coefficient on the composite blade is greater than that of the rigid blade, this is explained by the camber increase and the positive blade angle induced by the deformation. The local lift coefficient on the aluminum blade is overall a bit smaller than that of the rigid blade. It can be explained by the negative blade angle induced by the deformation, the camber increase seems to have a negligible effect here.

3.2 Vibro-acoustic phenomenon

For each blade, two vibro-acoustic computations were carried out: a first one on the initial configuration $\mathcal{C}_0$ and a second one on the intermediate configuration $\mathcal{C}_1$ taking into account the pre-stress and pre-strain of the propulsion phenomenon. The sound power is computed on the frequency $[100, 200]$ Hz. The computation on configuration $\mathcal{C}_0$ is the baseline and represents the acoustic signature of the blade without static load.

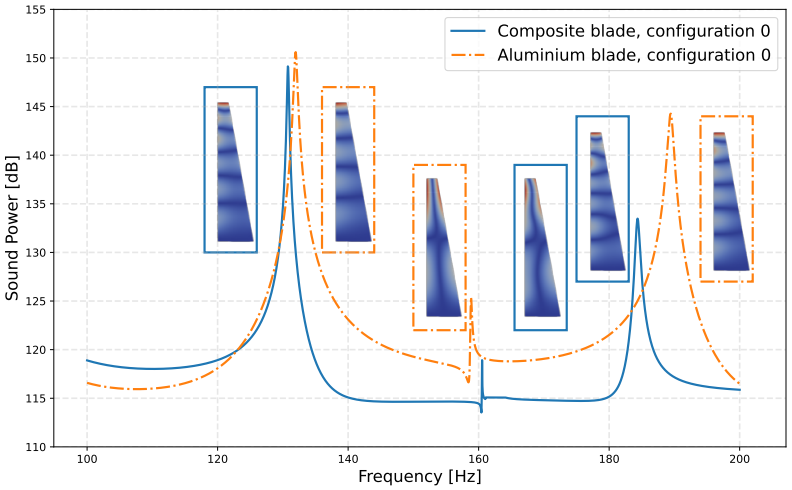

Figure 6: Sound power of the composite and aluminum blade, the displacement map for each modes are displayed. Computations are performed on the initial configuration $\mathcal{C}_0$ without pre-stress and without pre-strain

Figure 6 shows the sound power emitted in the fluid by the vibrating composite and aluminum blades in the initial configuration. At first glance, their vibrational characteristics seem similar, the peaks in the sound power are close in frequency and amplitude. The resonance peak around 160 Hz in Figure 6 corresponds to a 2^{nd} torsional mode for both the composite and the aluminum blades, therefore they have similar characteristics in torsion. However, the resonance peak around 135 Hz is a 6^{th} flexural mode for the composite blade and a 5^{th} flexural mode for the aluminum blade. Also, the resonance peak around 190 Hz is a 7^{th} flexural mode for the composite blade and a 6^{th} flexural mode for the aluminum blade. Therefore the composite blade is less rigid in flexion than the aluminum blade, this agrees with the deformation level observed from the static computations.

Figure 7 shows a comparison between the sound power emitted by the aluminum blade on configuration $\mathcal{C}_0$ and on configuration $\mathcal{C}_1$. On this figure, only the modes of the computation on $\mathcal{C}_0$ are displayed as they remain very similar on $\mathcal{C}_1$. Therefore sound power emitted by both blades are quite similar, the

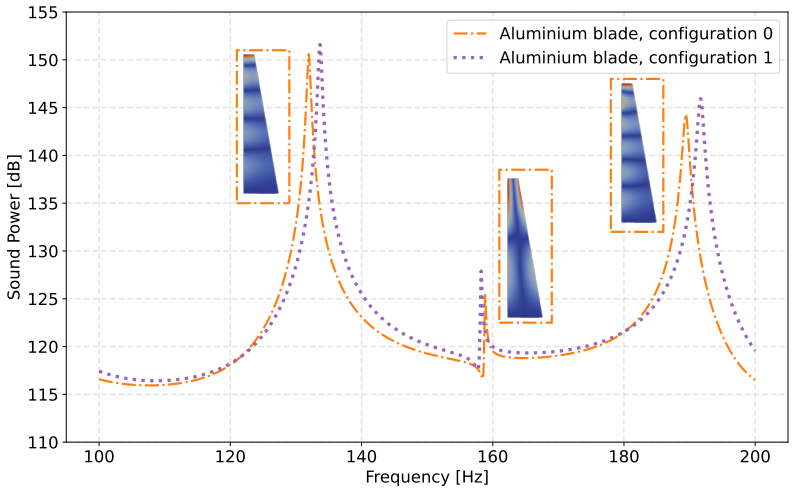

Figure 7: Sound power of the aluminum blade computed on configuration $\mathcal{C}_0$ (without pre-stress or pre-strain) and on configuration $\mathcal{C}_1$ (with pre-stress and pre-strain), the displacement map for each modes are displayed.

shift in frequency is less than 1.3% and there is less than 5 dB differences at the peaks. The flexural modes on the pre-stressed and pre-strained configuration $\mathcal{C}_1$ are shifted toward higher frequencies meaning that this configuration is a bit more stiff than the initial configuration $\mathcal{C}_0$. The power emitted by the blade on configuration $\mathcal{C}_1$ at the flexural modes is less than 3 dB higher, this difference would be hard to measure. The torsional mode's frequency is almost the same in both configuration however the power emitted is 5 dB higher which could be measured.

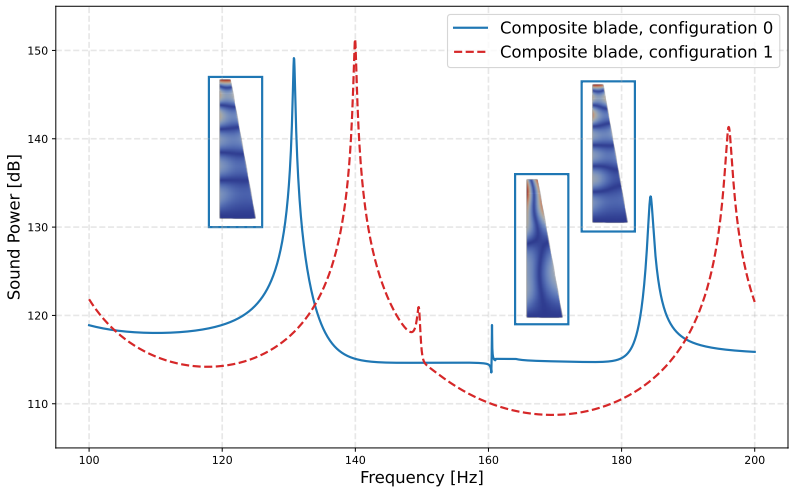

Figure 8: Sound power of the composite blade computed on configuration $\mathcal{C}_0$ (without pre-stress or pre-strain) and on configuration $\mathcal{C}_1$ (with pre-stress and pre-strain), the displacement map for each modes are displayed.

Figure 8 shows a comparison between the sound power emitted by the composite blade on configuration $\mathcal{C}_0$ and the blade on configuration $\mathcal{C}_1$. On this figure, only the modes of the computation on $\mathcal{C}_0$ are displayed as they remain very similar on $\mathcal{C}_1$. Both the first and third resonance peaks are flexural modes and both second resonant peaks are torsional mode. The sound power spectrums are fairly different:

there is a 8% shift toward higher frequency for the flexural modes and a 7% shift toward smaller frequency for the torsional mode on the configuration $\mathcal{C}_1$. These shifts in frequency are significant and could be measured. The amplitude of the third peak is 8 dB higher in configuration $\mathcal{C}_1$ than in configuration $\mathcal{C}_0$ which is significant. However the increase of power for the first two peaks is below 2 dB. As displacement and pre-strain are much more significant in the case of the composite blade, it seems coherent that the effect of the propulsion phenomenon on the emitted sound power is more important for the composite blade.

4. Conclusions

This approach aims at representing the physics of a vibrating rotating marine propeller deformed by its interaction with the incident flow. The large transformation of the structure, material non linearity and lift generation is called the *propulsion phenomenon*. The small linear vibrations of the pre-stressed and pre-strained propeller blades is called the *vibroacoustic phenomenon*. The cavitation and turbulence are not taken into account. The excitation source of the blades is simplified: a pressure oscillating at a given frequency is imposed on a fraction of the wetted surface. The simplified approach is mathematically proven within the hypothesis of this work. The propulsion phenomenon gives the pre-stress and pre-strain as input to the vibro-acoustic phenomenon which has no retro-action. Therefore, the two phenomena can be solved sequentially.

This approach is used to study the behavior of a composite blade and an aluminum blade. It appears that the composite blade suffers a significant deformation due to the incident flow, which has a positive effect on the lift generation along the blade as the camber increases and the angle blade is positive. This significant pre-strain and pre-strain leads to notable differences between the sound power emitted by the blade on the initial configuration and the intermediate configuration. On the other hand, the deformation of the aluminum blade due to the fluid flow is much smaller but it has a negative impact on the lift generation. As expected, this small deformation has a limited impact on the blade vibrational characteristics and the sound power emitted in configuration $\mathcal{C}_0$ remains close to that emitted on configuration $\mathcal{C}_1$

Therefore, the composite blades can be more flexible than their metallic counterpart and suffer large deformations under fluid load. However, these deformations can have a positive impact on the hydrodynamic performances and could be taken into account during the design phase to optimize its efficiency on a larger range of velocity and rotational speed. The deformed propeller can have different vibrational characteristics because of the pre-strain and pre-stress and a specific numerical approach such as the one presented in this paper is needed to computed its sound power.

ACKNOWLEDGEMENTS

We thank Astrid Filiot and Guillaume Dolo for the useful discussion regarding mechanics and software development. This study is financed by Naval Group and the ANRT through a doctoral study grant in collaboration with le Cnam.

REFERENCES

[Bayliss et al., 1982] Bayliss, A., Gunzburger, M., and Turkel, E. (1982). Boundary Conditions for the Numerical Solution of Elliptic Equations in Exterior Regions. *SIAM Journal on Applied Mathematics*, 42(2):430–451.

[Boncoraglio et al., 2021] Boncoraglio, G., Farhat, C., and Bou-Mosleh, C. (2021). Model Reduction

Framework with a New Take on Active Subspaces for Optimization Problems with Linearized Fluid-Structure Interaction Constraints. *International Journal for Numerical Methods in Engineering*, 122(19):5450–5481.

[Drela, 1989] Drela, M. (1989). XFOIL: An Analysis and Design System for Low Reynolds Number Airfoils. volume 54.

[EDF, 1989] EDF (1989). Finite element code_aster, Analysis of Structures and Thermomechanics for Studies and Research.

[Everstine, 1981] Everstine, G. C. (1981). A symmetric potential formulation for fluid-structure interaction. *Journal of Sound and Vibration, 79 (1), 157-160.*

[Glauert, 1935] Glauert, H. (1935). Airplane propellers. *Durand, W.F., Ed., Aerodynamic Theory, Vol. IV, Division L, Springer, New York*, pages 169–360.

[Leblond and Sigrist, 2016] Leblond, C. and Sigrist, J.-F. (2016). A reduced basis approach for the parametric low frequency response of submerged viscoelastic structures. *Finite Elements in Analysis and Design*, 119:15–29.

[Muller and Pécot, 2017] Muller, P. and Pécot, F. (2017). Development of a fluid structure coupling for composite tidal turbines and marine propellers.

[Rouleau et al., 2012] Rouleau, L., Deü, J.-F., Legay, A., and Sigrist, J.-F. (2012). Vibro-acoustic study of a viscoelastic sandwich ring immersed in water. *Journal of Sound and Vibration*, 331(3), 522–539.

[Taketani et al., 2013] Taketani, T., Kimura, K., Ando, S., and Yamamoto, K. (2013). Study on Performance of a Ship Propeller Using a Composite Material. *Third International Symposium on Marine Propulsors, Launceston, Tasmania, Australia.*